Hybrid additive manufacturing of Ti6Al4V with powder-bed fusion and direct-energy deposition

Simon Malej [a,b,e,*], Matjaž Godec [a], Črtomir Donik [a], Matej Balazic [b], René Zettler [c], Thomas Lienert [d], Laurent Pambaguian [e]

[a] Institute of Metals and Technology, Lepi Pot 11, 1000, Ljubljana, Slovenia
[b] Balmar D.o.o., Kidričeva Ulica 24A, 3000, Celje, Slovenia
[c] DIStech Disruptive Technologies GmbH, High-Tech-Park 24, A-8605, Kapfenberg, Austria
[d] Optomec, 3911 Singer N.E, Albuquerque, NM, 87109, USA
[e] European Space Research and Technology Center, Keplerlaan 1, 2201 AZ, Noordwijk, Netherlands

ARTICLE INFO

ABSTRACT

A single component can often benefit from being built using more than a single processing technique. Here, we investigated the hybrid additive manufacturing (HAM) of Ti6Al4V using a combination of powder-bed fusion (PBF) and direct-energy deposition (DED). The aim was to identify critical areas and assess the performance of the hybrid process relative to the individual processes. The PBF sub-parts were built first, and then completed by DED. The builds were in the horizontal and vertical directions, so we could observe the mechanical anisotropy relative to the build direction. X-ray computed tomography, microstructural examinations, and tensile testing coupled with digital image correlation were employed to assess the parts. The as-built PBF surface can be used to build HAM Ti6Al4V samples with DED, thus eliminating steps like machining. The HAM samples built in horizontally had intermediate tensile strengths of about 1050 MPa, and in the vertical direction, about 860 MPa, i.e., lower than the DED samples. Strength-wise, horizontally built parts exceeded the requirements. However, a reduction in deposition size (especially $<10^2$ mm^2) promoted a different temperature evolution and, in the worst-case scenario, heat accumulation, which led to the formation of an undesirable microstructure and local plastic deformation in the DED part.

1. Introduction

Hybrid additive manufacturing (HAM) combines the advantages of two technologies to give a product properties, capabilities, complexities, designs and repairs unavailable with a single technique [1]. It is usually a combination of additive manufacturing (AM) technology and conventional processes, like machining [2]. In some cases, 2 a.m. technologies [3] or a secondary process, like metal forming along with the AM process [3], are combined in a process chain. Many combinations have been researched. These include wrought + powder-bed fusion (PBF) [4], forged + wire-arc AM (WAAM)/metal forming (in-situ) [3], and PBF + WAAM [5].

The authors have previously combined PBF and direct-energy deposition (DED) [6–8] in a process chain to produce net-shape parts, such as the structural parts for space satellites. PBF can produce geometrically complex parts with good accuracy (0.01–0.5 mm) and

surface roughness (Ra = 7.8–11.1 μm [9] or higher [10]), good-to-excellent mechanical properties, and it has little need for post-processing (some machining of the functional surfaces, removing the dust from the surface and surface treatment are usually necessary) [11–14]. However, PBF is a relatively slow process (2–180 cm^3/h), while the size of the parts is limited by the size of the chamber where the part is built [13]. On the other hand, DED can produce semi-complex parts (without a support structure), achieve a high deposition rate of 125–500 cm^3/h, and involve larger chambers or no chamber at all (work volume limited by manipulation systems) [12,15–17]. The components built with DED tend to have poorer mechanical properties, a medium or lower accuracy (0.1–1 mm), and a higher surface roughness (Ra = 20–50+ μm) compared to components built with PBF [14,18]. The mechanical properties of DED tend to be lower than PBF due to larger average grain size, cell or dendrite spacing, more extensive segregation, and larger volume fractions of terminal solidification constituents

---

caused by slower cooling [19].

By combining PBF and DED, we aimed to fabricate medium-to-large-sized, optimized parts at a reduced manufacturing cost. The production of optimized parts could significantly reduce weight while maintaining the part's strength. Such a novel manufacturing principle represents a high implementation potential for various space applications where launch costs are very high (for launch into orbit, about 1.5–50k $/kg [20,21]). Furthermore, decreasing the system's complexity in terms of the number of parts shortens the time to delivery and lowers the total cost of the final assembly. In our previous paper, the HAM approach using PBF and DED was tested on Inconel 718 [6]. We found that the different microstructures of the DED and PBF parts and the thermal phenomena influenced the mechanical properties of the HAM parts [6]. Here, we report on a similar study using Ti6Al4V. Ti6Al4V has an excellent strength ratio to density and good corrosion properties [22]. It is often used in the space industry [23] (and similar applications) and could benefit from the HAM approach. The conventional production of Ti6Al4V parts is complex and expensive. The high price comes from the costly extractive and downstream processes [24]. Ti6Al4V is challenging to process with traditional methods like hot forming and machining. Consequently, manufacturing parts from Ti6Al4V using AM technologies is an attractive alternative. The manufacturing of Ti6Al4V parts using different AM technologies like PBF and DED has been extensively researched [25–28]. Combining both processes, as investigated here, has been limited to investigations of a flat interface, which is relatively straightforward because of the absence of defects [3–5]. PBF can produce high-strength parts thanks to the medium-sized, irregular, or columnar prior β-grains and α/α′ microstructure [29,30]. However, due to the α′/α phase, the elongation can be low. The α′/α microstructure is undesirable due to the parts' low elongation, fracture toughness, and fatigue performance. Therefore, annealing below the β-transus temperature (from 800 to 950 °C) is necessary after the PBF process [26]. Sub β-transus annealing transforms the α′/α microstructure into an α+β microstructure [25,26]. Similar prior β-columnar grains with an α/α′ microstructure form during the DED process as in the PBF. However, the prior columnar β-grains are usually much larger [28]. DED is a well-known process, generally used for repairs of high-value parts, and only a stress-relief heat treatment was performed after the DED of Ti6Al4V in previous studies [31]. This approach was necessary to prevent changes to the properties of the repaired parts. Since the resulting microstructures are roughly the same for PBF [30] and DED [28], the heat treatment of HAM Ti6Al4V could be less problematic, as was the case in a previous investigation conducted on Inconel 718 [6].

So far, only bulk samples in the vertical direction have been built and tested in different investigations [3–5,32]. However, the flat interface limits the complexity of the builds using the HAM approach. AM is intended to produce complex parts, which are typically impossible to do with typical processes. Therefore, this investigation aims to build samples in different orientations, considering the limitations of DED (geometry of the deposition head), perform mechanical tests, and compare the HAM samples with PBF and DED samples. Finally, we must explain the behavior of the HAM parts, emphasizing the results of tensile tests, microstructure examinations, and analyses of the defects.

2. Experimental

2.1. Manufacturing of the samples

The PBF involved powder provided by Praxair (Indianapolis, USA). The powder for the DED was supplied by AP&C (GE Additive Company, Boisbriand, Canada). The chemical compositions according to the powder producers of the PBF and DED powder are provided in Table 1. Table 2 shows the particle size distribution for the powder used in the PBF and DED. The particle size distribution was determined using a sieve method (ASTM B214). The flowability of the PBF powder according to ASTM B213 was <50 s, and the apparent density according to the DIN EN ISO 3923-1 standard was 2.43 g/cm^3. The powder for the PBF was recycled and reused. The powder was used only once as a virgin powder for the DED. The DED powder flow rate according to ASTM B213 was 25 s, and the tap density according to ASTM B527 was 2.59 g/cm^3. A titanium Ti–6Al–4V (Grade 5, ASTM B265) plate was used for the substrate (composition in Table 1). The composition of the substrate was measured with an XRF analyzer, Thermo Scientific Niton XL3t. Before the PBF, the base plate was cleaned with isopropanol and dried.

The PBF processing was conducted with a DISTECH (Kapfenberg, Austria) on a Trumpf TruPrint 3000 machine and the DED parts at Optomec (Albuquerque, USA) on an Optomec LENS 860 model machine. Separate PBF and DED samples were produced in conjunction with the HAM samples. The build direction in all cases was the Z (vertical) axis (Supplementary Fig. S1). Three different build orientations were built to examine the effects of build direction on crystallographic texture and mechanical properties. The orientations are referred to as (X, X+45, and Z), which indicate the axis in the coordinate system parallel to the long dimension of the sample. The PBF and DED samples printed in the X and X+45 orientations had a block shape with square cross-sections with dimensions of 65 × 10 × 10 mm^3. The X+45 build orientation indicates a horizontally placed block that is rotated 45° around the Z axis. In the Z orientation, the samples had a cylindrical shape with dimensions of 65 × Ø10 mm^2. The HAM process (Fig. 1a–j)) involved three critical steps.

1) Manufacturing of sub-parts by PBF: In the X and X+45 orientations, the PBF sub-parts had a wedge shape with the dimensions provided in the Supplementary Fig. S1a. The wedge shape allowed clearance for the DED laser deposition head (the diameter of the DED deposition head is roughly 80 mm, and the standoff distance is 11 mm). The inclined surface of the wedge enables easier deposition, decreases the likelihood of defect formation, and prevents collision of the DED laser head with the samples during manufacturing. In addition, no contour parameters were used to minimize the influence of contour parameters on the interface properties. Examples of finished HAM X and HAM X+45 PBF subparts are presented in Fig. 1a). The HAM Z PBF sub-parts built in the Z direction had cylindrical shapes, as

Table 2
Particle size distribution of PBF and DED powders.

Process	Particle size [μm]		
	D10	D50	D90
PBF	19	33	49
DED	54	81	123

Table 1
Chemical compositions of the PBF and DED powder and substrate.

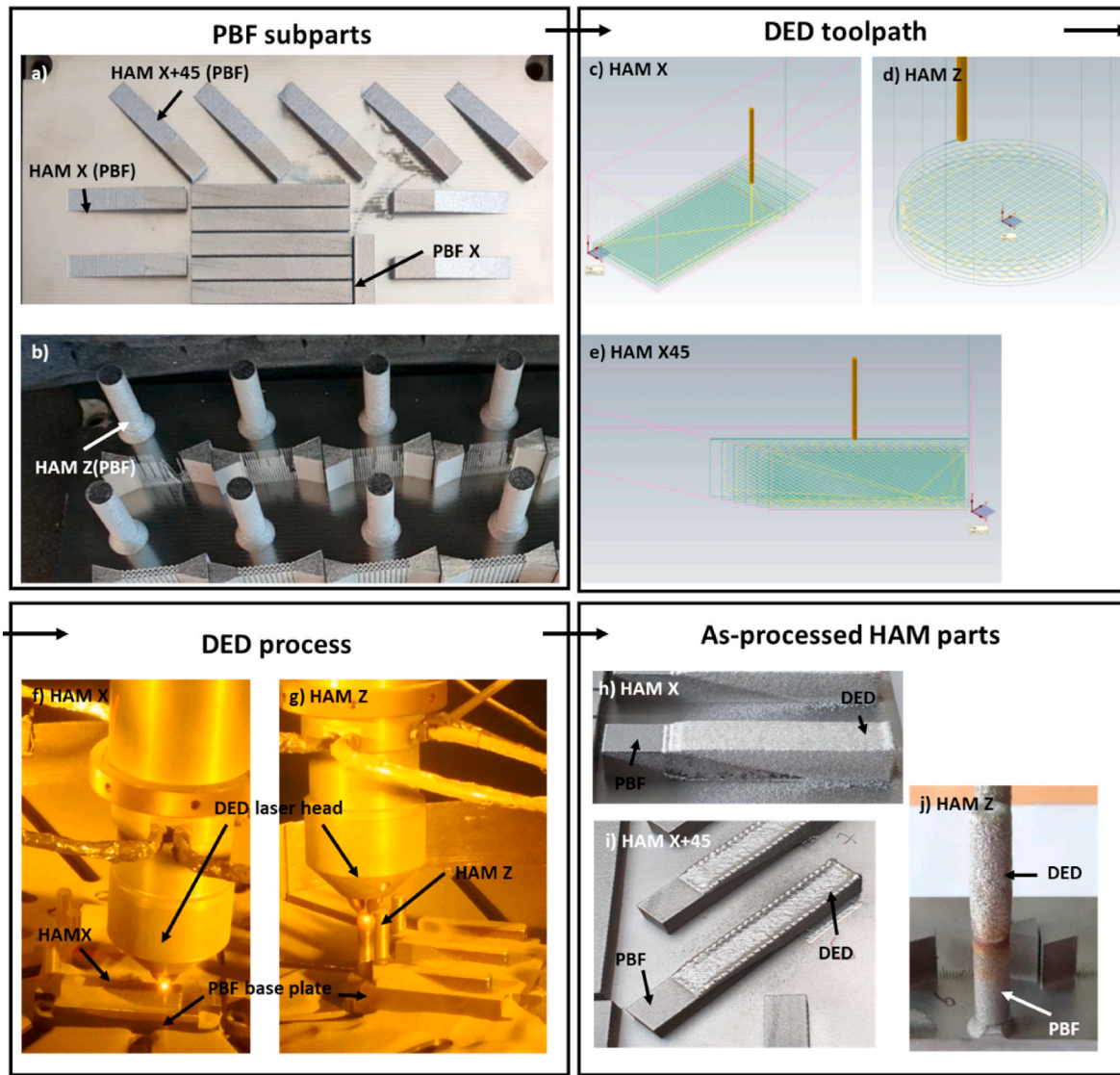|	%H	%C	%O	%N	%Al	%Fe	%V	Ti
PBF	0.002	0.13	0.16	0.0218	6.13	0.93	3.9	Balance
DED	0.002	0.01	0.1	0.03	6.33	0.07	3.98	Balance
Substrate	–	–	–	–	5.54	0.12	4.03	Balance

Fig. 1. Shows important steps in the HAM part's manufacturing. The as-build HAM X and X+45 PBF subparts are shown in Figure a) and HAM Z in c). Figure a) also show the full PBF X part. The upper left quadrant shows the toolpath for the first 5 DED layers of HAM X a), HAM X+45 b), and HAM Z c) parts. Images on the lower left quadrant show an example of the DED process during the manufacturing of the HAM X a) and HAM Z b) samples (provided images are not from the processing of Ti6Al4V). The last quadrant shows finished HAM X a), X+45 b), and Z c) samples after DED.

shown in Fig. 1b). The finished HAM Z PBF subparts are shown in Fig. 1b).

2) Preparation for DED processing: Before DED, no post-processing of the PBF sub-parts was conducted, e.g., heat treatment, machining, or cleaning. The reasons are less surface contamination by machining and tedious cleaning after machining. Furthermore, the as-built PBF surface is less reflective than the machined surface. The PBF sub-parts remained on the build plate and were stored in a sealed box to prevent surface contamination during transport and preparation for the DED.

3) DED of HAM samples: DED processing of the HAM X and X+45 samples was conducted on the build plate and partially on the in-clined surface of the PBF sub-part. The laser scanning path (The DED tool path) for HAM X and HAM X+45 is presented in Fig. 1c) and e), respectively. The tool path for HAM X always followed either the x or y-axis direction (Fig. 1c)). In contrast, the tool path for HAM X+45 samples was always at a 45° angle relative to the x or y-axis (Fig. 1e)). An example of the DED process of HAM X samples is shown in Fig. 1f). The building of the HAM samples using DED in the Z orientation continued from the surface where the PBF process

finished (Fig. 1d) and c)). An example of DED of HAM Z manufacturing is shown in Fig. 1g). Finished HAM X, HAM X+45, and HAM Z samples are presented in Fig. 1h), i) and j), respectively.

Table 3 summarizes the relevant process parameters for the PBF and DED. The process parameters in Table 3 are standard, provided by the machine manufacturers. The exact process parameters were used for the

Table 3
Process parameters for PBF and DED.

Process	PBF			DED		
Orientation	X	X+45	Z	X	X+45	Z
Power [W]	280			380		360
Scan speed	1200 mm/s			1016 mm/min		
Layer thickness [mm]	0.03			0.305		
Hatch spacing [mm]	0.14			0.457		
Rotation of each layer [°]:	67			90		
Powder flow rate [g/min]	Not relevant for PBF			2.15		
Laser beam diameter [mm]	0.1			1.0		
Chamber atmosphere	Argon			Argon (O$_2$ 5.3 ppm)		

HAM samples.

Chemical analyses were performed on the as-built samples using ICP-OES (Inductively coupled plasma–optical emission spectrometry, Agilent 720). The carbon was analyzed with an ELTRA CS800, while oxygen and nitrogen were analyzed with an ELTRA N900 analyzer. Table 4 shows the chemical composition of the Ti6Al4V parts according to the ASTM F2924-14 standard and the chemical analyses of the as-built DED and PBF parts.

After the PBF, DED, and HAM, the samples were cut off the base plate with wire-electrical-discharge machining. The samples were heat treated in a resistance furnace in the air to remove the α′ microstructure. Annealing was conducted at 800 °C for 2 h (preheated furnace), and the furnace cooled (the cooling rate from 800 to 300 °C was about 64 °C/h). After heat treatment, the majority of the samples were machined by CNC to produce circular tensile probes with M8 threads (DIN 50125 ″B 5 × 25). The remaining samples were used for material characterization.

2.2. Material characterization

Density measurements based on Archimedes' principle were performed on each tensile probe using a Sartorius RC210S scale with the YDK 01 density-determination kit and absolute ethanol (CAS No.: 64-17-5). The samples submerged in the ethanol were degassed in a vacuum chamber before the measurements to eliminate any bubbles. On the two HAM samples (HAM X and HAM X+45) with the lowest density, X-ray computed tomography (CT) was performed on a General Electric Vtome x m300 and analyzed with VGstudiomax 3.4 software.

Micro-sections were prepared for each sample made with different technology and direction of printing. The micro-section samples were molded in EpoFix (Struers epoxy). Preparation of the micro-sections involved grinding (FEPA-P180, P320, P500, P800, P1200, P2400, and P4000 grit size, SiC), polishing (6 and 3 μm, diamond), and final polishing with OP-S (Colloidal suspension of silica with a grain size = 250 nm). Peroxide was added to the OP-S (2%) to achieve combined chemo-mechanical polishing. Samples for the microstructure investigations were etched with Kroll's reagent. Light microscopy (LM) and scanning electron microscopy (SEM) of the samples were performed with a Leica DVM6 optical microscope and a Carl Zeiss Cross Beam 550 SEM, respectively. Additionally, electron backscatter diffraction (EBSD) of the HAM samples was performed on the Carl Zeiss Cross Beam 550 SEM (EDAX Hikari Super EBSD camera with TEAM software and TSL OIM Analysis 8 software). EBSD mapping was conducted with an accelerating voltage of 15 kV, step size of 1 μm, working distance of 18.7 mm, and the specimen was tilted for 70°. Lath/lamella thickness was measured to quantify the differences between different microstructures (PBF, DED, and HAM (PBF and DED)) using the program ImageJ 1.53k. The measurements were conducted on LM images where 50 laths were measured. The average and standard deviation of the lath thickness were calculated from the measured data.

2.3. Mechanical testing

The tensile tests were performed on a Zwick Z100 tensile-testing machine equipped with a 100-kN load cell. A constant strain rate of 2.5×10^{-4} s^{-1} was used during the tensile test. The specimens were clamped using steel mounting adapters with an M8 threaded hole. The test apparatus, specimens, test procedures, precision, and bias, conformed with EN ISO 6892. For each technology and orientation, 3–7 tensile specimens were tested (DED 3 while for PBF and HAM 7). The test parts were selected according to the DIN 50125:2009–07 standard for type-B test pieces. A GOM Aramis SRX was used for an optical 3D measurement of the strains on the observed surface of the tensile specimens. The GOM Aramis SRX system included controlled light sources via the GOM testing controller, an ARAMIS adjustable base, a high-performance computer, and the application software ARAMIS Professional Live. The pattern was applied with white acrylic paint (DUPLI-COLOR AQUA Lackspray) and black paint with graphite particles (GRAPHIT 33, Aerosol). The setup for the digital image correlation included GOM Aramis Titanar B75 mm lenses, the camera's measuring volume was $50 \times 40 \times 10$ mm^3, the cameras were attached to a 500/800 frame, the measuring distance was 325 mm, the slider distance was 110 mm, the calibration object was CP40/MV60, the distance ring was 25 mm, the dual LED lighting and frame capture was 1 Hz. The fracture surfaces were imaged with a Leica M80a stereomicroscope, a Leica Dmi8 microscope, and a Carl Zeiss EVO60 scanning electron microscope.

2.4. Statistical evaluation of data

Due to many data and to see interdependencies (between the technologies and orientation of printing) more clearly, we wrote Python code where we used SciPy to perform a *t*-test [33] and matplotlib [34] to generate a graphical plot. To perform the *t*-test we used the ttest_ind function [35]. Two different configurations were used. When the number of samples between group 1 and group 2 was the same and ratio between the variances of group 1 and group 2 was less than 4 we used the standard independent 2 sample test (equal_var = True). Otherwise, we performed Welch's *t*-test (equal_var = False). The means of group 1 and group 2 were regarded as different if the p-value was less than 0.05. The t and p values were calculated for every combination and plotted in the graphical plots where in each square two values are present (the top value is p and the bottom t). Green square means there is no significant difference in means and the other way around if the square is red. A negative t-value means that the mean of group 1 on the vertical axis is smaller than the mean of group 2 on the horizontal axis. The *t*-test was implemented for alpha lath thickness, and tensile test results.

3. Results

3.1. Density measurements of tensile probes

Archimedes density measurements were conducted on all the tensile samples to check for potential defects in the manufactured parts (Fig. 2). The average density of the DED samples is between 99.82 (X+45) and 99.90% (X), and for PBF samples, from 99.79 (Z) to 99.95% (X). However, the average density of the HAM samples was considerably lower (from 99.57 (Z) to 99.68% (X)). The lowest density of the HAM samples was observed in one of the HAM X+45 samples (99.51%). In the HAM X and X+45 group, some samples showed a considerably lower Archimedes density than the group average. The deviation in density compared to the average could indicate the high probability of a defect. Therefore, one sample with the lowest density was chosen from group HAM X (99.61%) and HAM X+45 (99.51%) for CT analyses (see next

Table 4
Chemical composition according to the ASTM F2924-14 standard for PBF and chemical analyses of the DED and PBF parts.

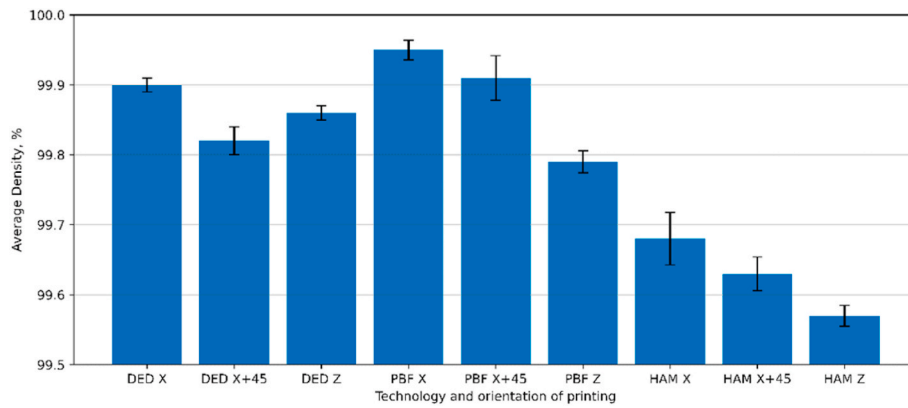|		%C	%O	%N	%Si	%S	%Cr	%Cu	%Mo	%Ni	%Al	%Fe	%V	%Y	Ti
ASTM F2924-14	Min.	–	–	–	–	–	–	–	–	–	5.50	–	3.50	–	a
	Max.	0.08	0.2	0.05	–	–	–	–	–	–	6.75	0.30	4.50	0.005	
PBF		0,011	0,13	0,021	0018	0,002	< 0,01	0,011	<0,01	0,015	6,2	0,15	4,0	–	a
DED		0,078	0,13	0,045	<0,010	0007	0,02	0,020	<0,01	0,015	6,4	0,26	3,9	–	a

^a Balance.

Fig. 2. Average Archimedes density of DED, PBF, and HAM Ti6Al4V parts built in the X, X+45, and Z orientations.

Section 3.2).

3.2. X-ray computed tomography of samples with low density

CT was performed for the HAM X and X+45 samples with the lowest density. Fig. 3a and b) (HAM X) and Fig. 3c and d) (HAM X+45) show CT scans of tensile specimens with highlighted defects at the PBF/DED interface. According to the CT scans, two types of defects can be observed near the PBF/DED interface. The first type is small (<0.5 mm diameter, Supplementary Figs. S4a and b)), discrete, and nearly spherical (colored blue in Fig. 3a and b) and Fig. 3c and d)). They can be observed along the entire PBF-DED interface and into the DED deposit. The origin of the small-scale defects is probably the entrapment of gas bubbles that cannot escape before solidification, as known from welding [36]. They likely resulted from oxides on the PBF surface, perhaps containing moisture picked up during shipping or from contamination by the packaging material. The second type of defect is extended, follows linear paths parallel to the hatch direction, and results from lack-of-fusion. The lack-of-fusion defects (often triangular tunnels with unbonded powder) derive from insufficient hatch or z-step spacing and low heat input. The HAM X sample in Fig. 3a) shows extended defects, spanning the cross-section of the tensile specimen. The shape of the macro defects in the HAM X+45 sample (Fig. 3d)) is different from the HAM X sample in terms of size and shape. The positioning of the defects is connected to the scanning strategy. In both cases (X and X+45 orientations), the small-scale defects and the lack-of-fusion defects follow the inclination of the wedge (Fig. 3a and b) and Fig. 3c and d)). The mean diameter size of the pores is larger in the HAM X (Supplementary Fig. S4a)) parts compared to HAM X+45 (Supplementary Fig. S4b)).

3.3. Microstructure investigation of PBF, DED, and HAM samples

PBF and DED samples (Fig. 4a–f) have, after heat treatment, fine α+β microstructures. The α-phase adopted an acicular or lath shape with a similar thickness (Supplementary Fig. S2, except HAM(DED) Z). A detailed analysis shows in some instances larger lath size of PBF Z and
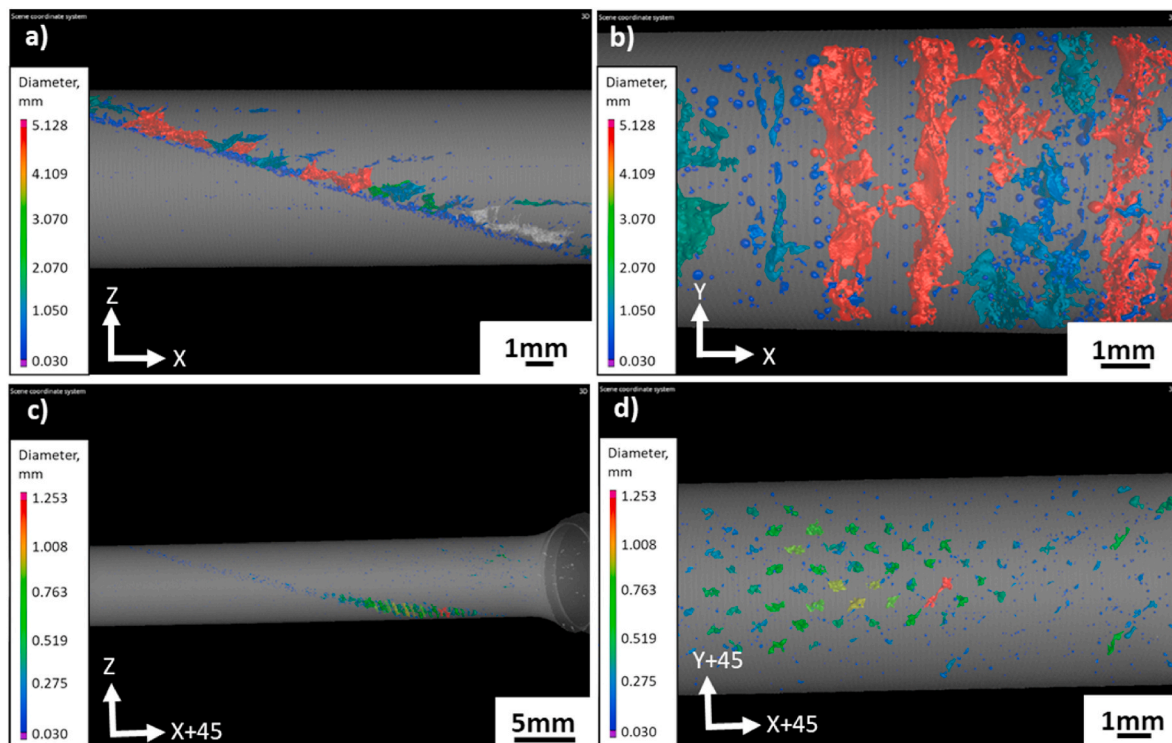

Fig. 3. CT images of HAM X (a) and b)) and HAM X+45(c) and d)) samples with significant lack-of-fusion defects and more minor defects at the PBF/DED interface view from the side and plan view, respectively.
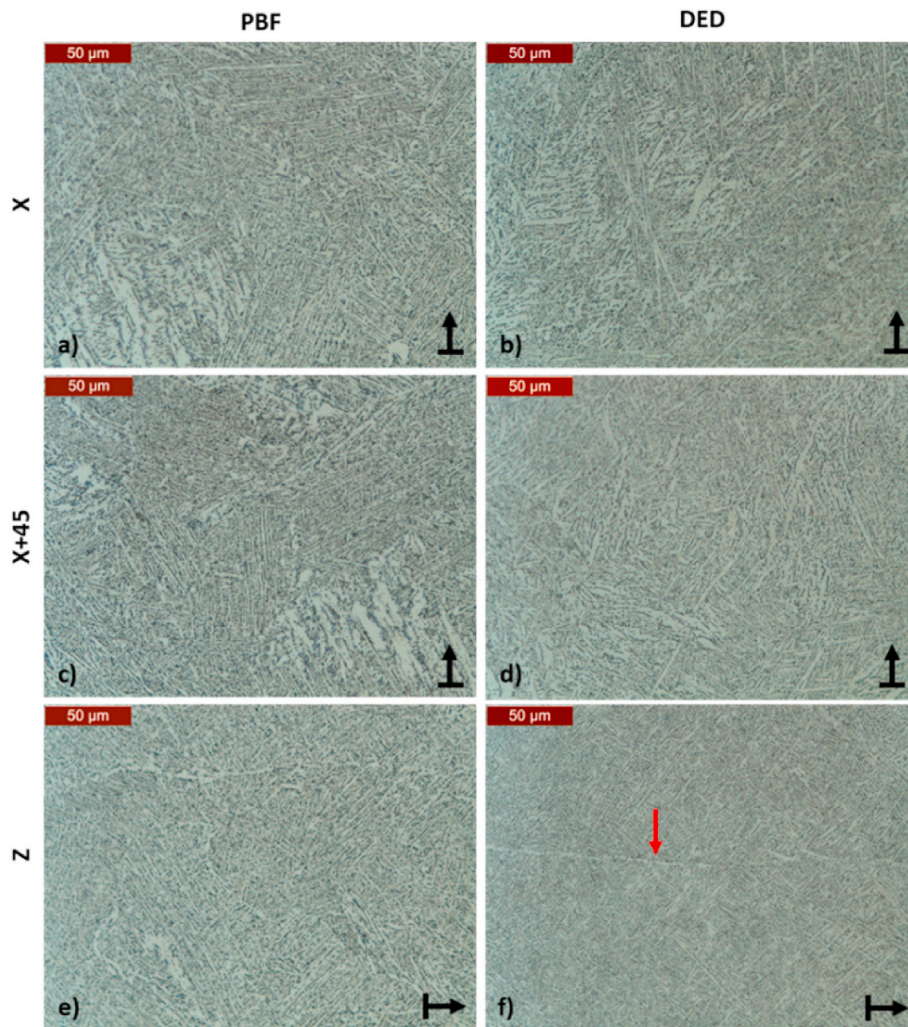
Fig. 4. LM images at 500 × magnification of microstructures from PBF X a) PBF X+45 b), PBF Z c), DED X a) DED X+45 b), and DED Z c) sample.

HAM(DED) X+45 parts compared to others (Supplementary Fig. S3). In addition, DED Z samples have highlighted prior β-grain boundaries with an α-phase (α-grain boundary, Fig. 4f) red arrow). In contrast to PBF and DED samples, HAM X and HAM X+45 samples (Fig. 5a–d)) show some additional features. Some prior β-grain boundaries on the DED side have a layer of α-phase in the HAM X and X+45 samples (Fig. 5b) red arrow). The α-phase along the grain boundary on the DED side of HAM X samples (Fig. 5b)) appears to be thicker in comparison to the DED Z samples (Fig. 4f)). The average lath size in HAM X and X+45 is similar (Supplementary Fig. S2) to PBF and DED samples. The HAM Z samples, on the other hand, have entirely different microstructures (Fig. 5e and f)). The DED side of the HAM Z samples (Fig. 5f)) has a coarse α+β microstructure with large colonies of thick α-lamella and α-phase along the prior β-grain boundary (HAM(DED) Z, Supplementary Fig. S2). A coarse α+β microstructure formed due to heat accumulation from 1-D heat flow during the build.

The approximate location of the interface between the PBF and DED part in the HAM X (Fig. 6a)) HAM X+45 (Fig. 6b)) and HAM Z (Fig. 6)) can be identified based on the changes in the grain morphology. The PBF samples have small prior β-grains with an irregular or columnar appearance (Fig. 6a–c)). On the other hand, the DED samples have large columnar prior β-grains that extend through multiple deposition layers (Fig. 6b)). Texture is stronger in the DED (Supplementary Fig. S5) parts relative to PBF (Supplementary Fig. S6). The prior columnar β-grains have a wavy appearance because the prior columnar β-grains tend to grow towards the heat source during the solidification. At the PBF/DED

interface, a transition can be seen where the smaller prior β-grains on the PBF side transition to large columnar prior β-grains on the DED side (Fig. 7c)). EBSD of the HAM X sample PBF/DED interface showed slightly angled columnar prior β-grains toward the interface, compared to PBF (Fig. 7a)) and (Fig. 7b)) DED side. Columnar prior β-grains are angled due to heat transfer to the PBF/DED interface. For HAM XY (Fig. 6) and HAM XY+45 X (Fig. 6b)) a heat-affected zone (HAZ) is very narrow and not visible at optical magnifications and according to EBSD, at the PBF/DED interface (Fig. 7c)). EBSD of the PBF/DED interface showed only a transition from PBF to DED grain structure. HAM Z (Fig. 7c)) samples have a sizeable heat-affected zone on the PBF side, roughly 3 mm in size. The heat-affected site is roughly composed of two parts (Supplementary Figs. S7a and b)). The lower area (toward the PBF side) of the heat-affected zone is composed of short and thick α-laths (Supplementary Fig. S7a). In contrast, the upper part (closer to the DED side) comprises colonies of α-lamella and α-phase along the prior β-grain boundaries (Supplementary Fig. S7c)). The first few depositions layers on the DED side of the HAM Z sample are characterized by two large prior-β columnar grains on the edge of the micro-section and multiple small grains in the center (Fig. 6c), red arrow). After some deposition layers (8–9 mm from PBF/DED interface), smaller columnar grains in the center transition to larger columnar prior β-grains.

On a much smaller scale (SEM investigation), clearly defined α-laths can be seen on both the PBF and DED samples (Fig. 8a–d)). At the border of the α-laths, the β-phase can be seen. In the electron channel contrast images (ECCI), the β-phase is colored white due to the higher content of
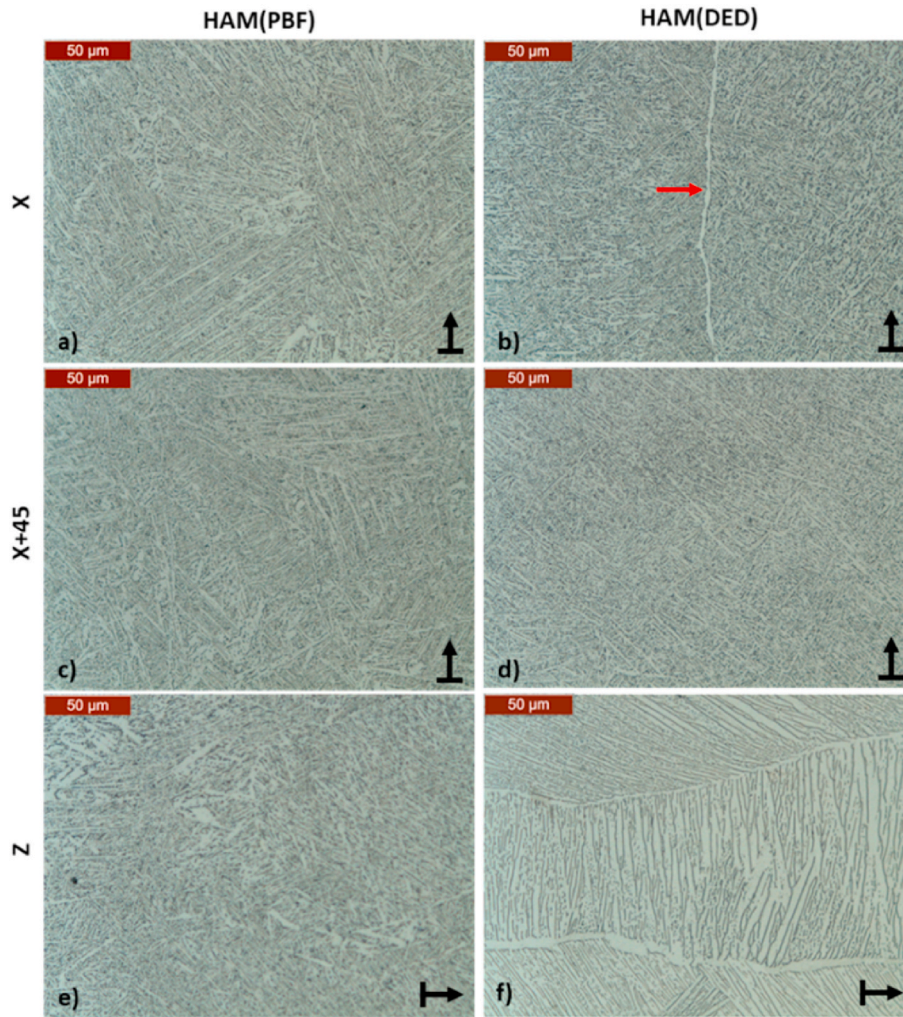
Fig. 5. LM images at 500 × magnification of microstructures from HAM X PBF side a) and DED side b), HAM X+45 PBF side c) and DED side d) and HAM Z PBF side e) and DED side f).

V with a higher atomic weight. ECCI is a surface analysis technique used in the SEM microscope and is based on the electron channeling effect by applying backscattered electrons. Microstructures from the PBF (Fig. 8a and b)) and DED (Fig. 8c and d)) sides appear very similar.

3.4. Hardness measurements across PBF/DED interface of HAM samples

Three hardness profiles altogether were measured across the PBF/DED interface of HAM X, HAM X+45, and HAM Z samples (Fig. 9a–c)), to identify the location of the PBF/DED interface and the heat-affected zone. The results are shown in Fig. 9, where three Vickers hardness profiles for each sample were measured normal to PBF/DED interface for HAM X a), HAM X+45 b), and HAM Z c) samples. The hardness profile on the left-hand side of the PBF/DED interface pertains to the DED side. In contrast, the right-hand side relates to the PBF side, and the middle (0 mm) indicates the approximate location of the interface based on the stereomicroscopic images (Fig. 6a–c)). The hardness measurements for (a) HAM X and (b) HAM X+45 show considerable spatial scatter on both the PBF and DED sides, evidently dependent on the local phases encountered by the indenter. Consequently, general hardness trends are difficult to resolve, although the hardness values fall consistently within a band between 360 and 375 HV0.1. The hardness profiles of the HAM Z (Fig. 9c)) samples show clearly defined heat-affected zones. About 3 mm before the interface, the hardness of the PBF side starts to drop from around 370 to 330 HV0.1 (at around 0.25 mm) before

rising steadily and reaching a consistent value near 370 HV0.1 at ~ 3 mm from the interface. On the DED side, a large spread in hardness values was encountered. Despite this, the Vickers hardness on the DED side of HAM Z samples is lower (around 330 HV0.1) compared to the DED side of the HAM X and X+45 samples. Lower hardness on the DED side is connected to the rough α+β microstructure consisting of thick α-lamella colonies (Fig. 5f)) caused by heat accumulation.

3.5. Influence of the HAM approach on the tensile properties

Typical tensile curves of PBF, DED, and HAM samples are presented in Fig. 10a-c). Fig. 11 shows the average yield strength, tensile strength, strain at fracture, uniform strain, and modulus of elasticity for the PBF, DED, and HAM samples built in the X, X+45, and Z directions. The tensile properties of the DED samples show a trade-off between yield strength and tensile strength on the one hand, and strain at fracture, on the other (Supplementary Figs. S8 and 9). The DED samples built in the X orientation show the highest yield strength (1034 ± 2.7 MPa) and tensile strength (1101 ± 4.0 MPa), and the lowest average strain at fracture (8.9 ± 0.7%). On the other hand, the average yield strength and tensile strength were the lowest for the DED samples built in the Z direction (932 ± 8.3 and 1028 ± 6.6 MPa, respectively), while the strain at fracture in the Z samples (12.2 ± 1.1%) was the highest. The DED process shows considerable anisotropy in the mechanical properties given the orientation of the build. The average tensile properties for the
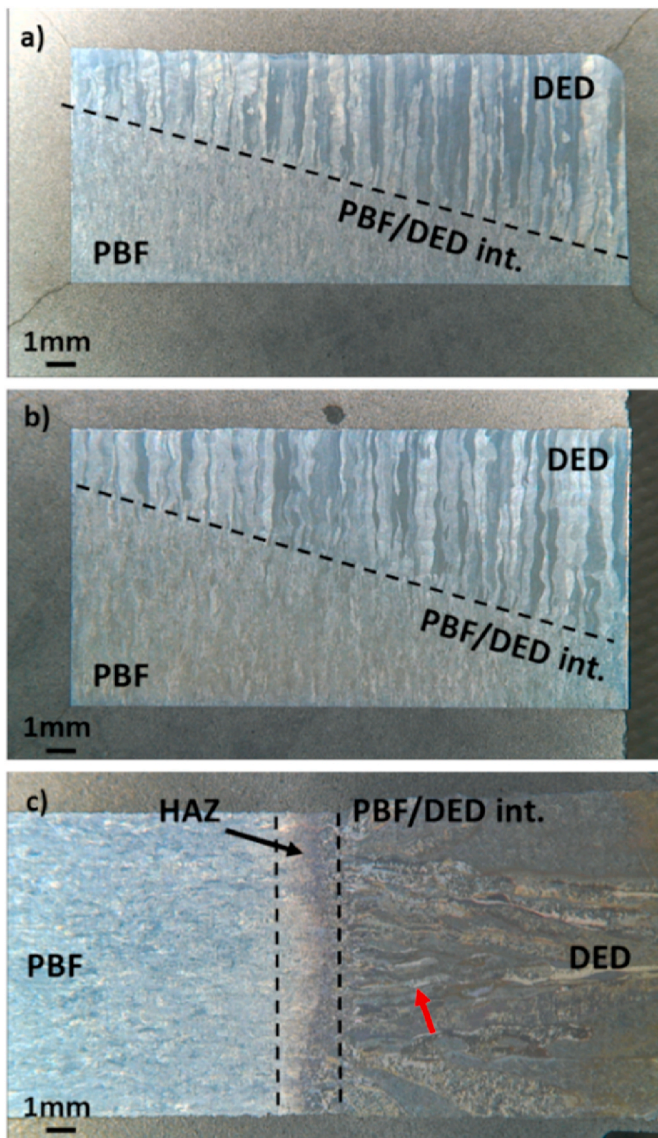
Fig. 6. Stereoscope image of the macrostructure a) at the PBF/DED interface of HAM X b) HAM X+45 b), and c) HAM Z sample (int. indicates interface).

DED samples (yield and tensile strength, and strain at failure) exceeded those stipulated by the ASTM standard [37] except for the strain at failure for the X orientation samples (Fig. 11, upper three rows).

The PBF samples built in the X, X+45, and Z directions show similar (Supplementary figure S8-10 and 12) average strain at fracture, moduli of elasticity and yield, and tensile strengths (around 117 GPa, 1020, and 1084 MPa, respectively). The anisotropy in the mechanical properties was less noticeable in the PBF samples. The average yield and tensile strength, and strain at fracture of the PBF samples exceeded those for the ASTM F2924-14 standard in all orientations (Fig. 11, middle three rows). Interestingly uniform strain of DED and PBF parts is similar between orientations except for the DED Z (Fig. 11 and Supplementary Fig. S11).

The HAM X has a slightly higher average modulus of elasticity, yield strength, and tensile strength than HAM X+45 parts. The strain at fracture and uniform strain of the HAM X and X+45 was considerably lower than for the PBF and DED samples (Fig. 11 and Supplementary Fig. S11). The average strain at fracture of the HAM samples built in the X+45 direction (7.7 ± 0.7%) is higher than those made in the X direction (6.0 ± 1.7%). Some of the HAM samples built in the X, X+45 directions show very low strain at fracture (around 1–2%). The same

samples had lower than average Archimedes density and exhibited lack-of-fusion defects on the DED side of the PBF/DED interface (HAM X Fig. 3a and b) and HAM X+45 Fig. 3c and d)). There were two samples with low strain at fracture for the HAM X samples, while for the HAM X+45 samples, there was only one. These reasons provide at least a partial explanation for the lower average strain at fracture for the HAM X and X+45 samples.

3.6. LM of tensile samples after fracture

Microsections were prepared from fractured tensile specimens (Supplementary Figs. S13a and b)) to identify the location of the fracture and the state of the PBF/DED interface in the HAM parts. In most cases, the rupture of the HAM samples occurred away from the PBF/DED interface. A dashed red line designates the approximate location of the interface on the HAM X (Supplementary Fig. S13a)) and HAM Z samples (Supplementary Fig. S13b)). The fracture of the HAM X (Supplementary Fig. S13a)) sample occurred shortly after the transition to the full DED part. The PBF/DED interface can be seen due to the grain morphology difference and some defects. The fracture of the HAM Z (Supplementary Fig. S13b)) sample occurred about 7.5 mm away from the PBF/DED interface.

3.7. Fracture surface analysis

Comparing stereomicroscope and SEM micrographs of the fracture surfaces highlighted some significant deviations between different technologies (Fig. 12, Supplementary Fig. S10, and Fig. 13). Fig. 12a–i) shows stereomicroscope images of the fracture surface from the PBF, DED, and HAM samples in the X, X+45, and Z orientations. The PBF samples had a rough surface with a typical cup-shaped fracture, indicating ductile failure (Fig. 12a, d, and g)). The fracture surface of the DED samples revealed different characteristics. The bands on the DED samples built in the X (Fig. 12b)) and X +45 (Fig. 12e)) orientations can be seen. The same bands were not observed on the DED Z (Fig. 12h)) samples (the fracture features were like the PBF samples). The same bands observed on the DED X and X+45 samples were also on the HAM samples built in the X (Fig. 12c)) and X+45 (Fig. 12f)) samples. There were exceptions; in a small number of samples, major lack-of-fusion defects formed (Fig. 3a) and b) and Supplementary Fig. S14). In that case, the fracture occurred across the PBF/DED interface. Furthermore, from Supplementary Fig. S14, the bands are oriented in the building direction, as they are oriented perpendicular to the linear lack-of-fusion defects.

SEM micrographs of the fracture surface from the PBF, DED, and HAM (X and X+45) samples revealed very small, shallow dimples (Fig. 13a–f)). The dimples have a similar size for the different processes (PBF, DED, and HAM (X and X+45)). The main difference is in the shape and distribution of the fractures across the prior β-grain boundaries. These features are observed in the PBF and DED samples to a small extent. However, in HAM (X and X+45) samples, fractures across prior β-grain boundaries appear more common due to the parallel steps on the fracture surface (Fig. 13e and f)). In contrast to the PBF, DED, and HAM (X and X+45) samples, the HAM Z samples do not share any common features. The fracture surface of the HAM Z samples is rough (Fig. 13i)), with large shallow dimples and quasi-brittle areas (Fig. 13g and h)).

3.8. Digital image correlation during tensile tests of PBF, DED, and HAM samples

On all the samples, digital image correlation was used to observe the strain distribution during the tensile test (Fig. 14a–c). Three distinct behaviors were observed, excluding samples with lower-than-average strain at fracture (samples with extensive defects). The first case includes samples fully built with a single technology (PBF or DED). Fig. 14 shows the strain distribution on the PBF X tensile sample before fracture.
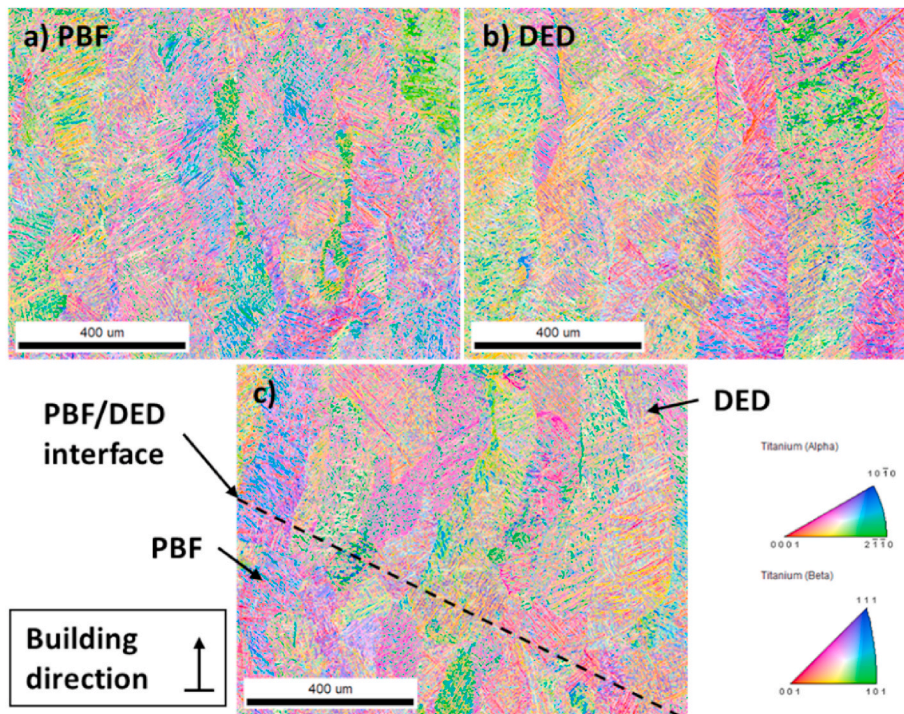
Fig. 7. EBSD images with IPF-Z coloring of a) HAM X sample on PBF side b) DED side b) and c) at the interface between PBF and DED.
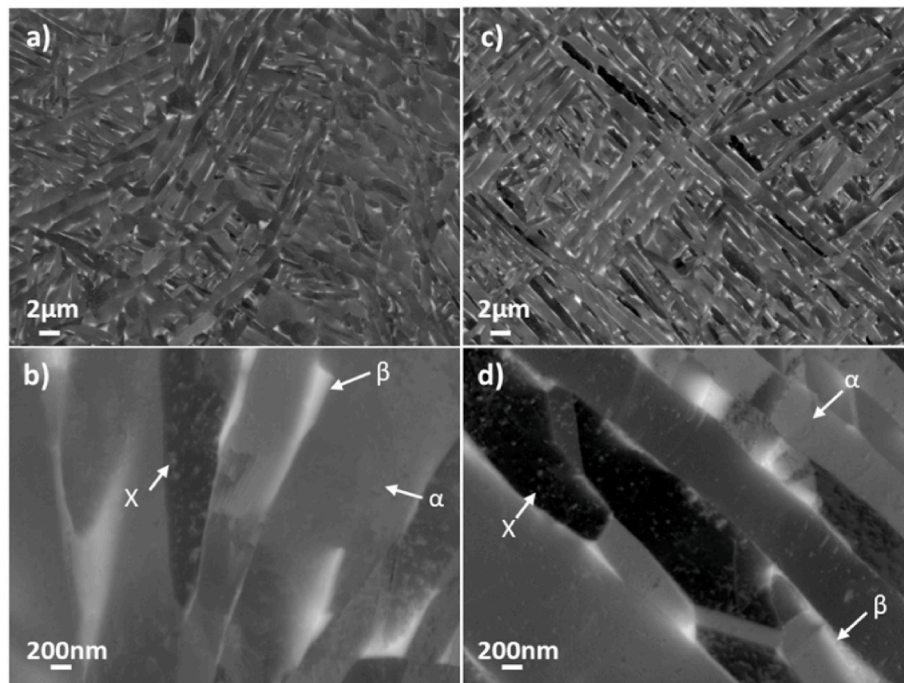

Fig. 8. Electron channel contrast images of HAM X sample on PBF side a,b) and DED side c,d). The X denotes internal defects like dislocations.

From four points along the length of the probe, local strain evolution vs. nominal strain was plotted (Fig. 15a–c)). For the PBF X sample (Fig. 15a)) three typical areas are observed: elastic region (linear part), the start of plastic deformation in the gauge area (at the yield point), a transition to necking (points 1–4 start to split, Fig. 15a)), which ends with fracture of the part at point 3. Note the development of diffuse strain bands oriented at ±45° to the loading direction where the maximum resolved shear stresses develop and no significant defects exist.

In HAM samples, (HAM X Fig. 14b), the DED part with the lowest yield strength starts to yield first, including the transition area near the PBF/DED interface. Therefore, there is localized plastic deformation on the DED side of the tensile probe gauge length, which is different compared to the PBF (Fig. 15a)) and DED samples. Necking of HAM samples starts with the yield point of the DED part. The PBF part will start to yield later when the engineering stress reaches the yield point of the PBF part. The elastic region of point 4 (PBF side, Fig. 14b)) of the HAM X sample is extended. According to the tensile data (Fig. 11), the
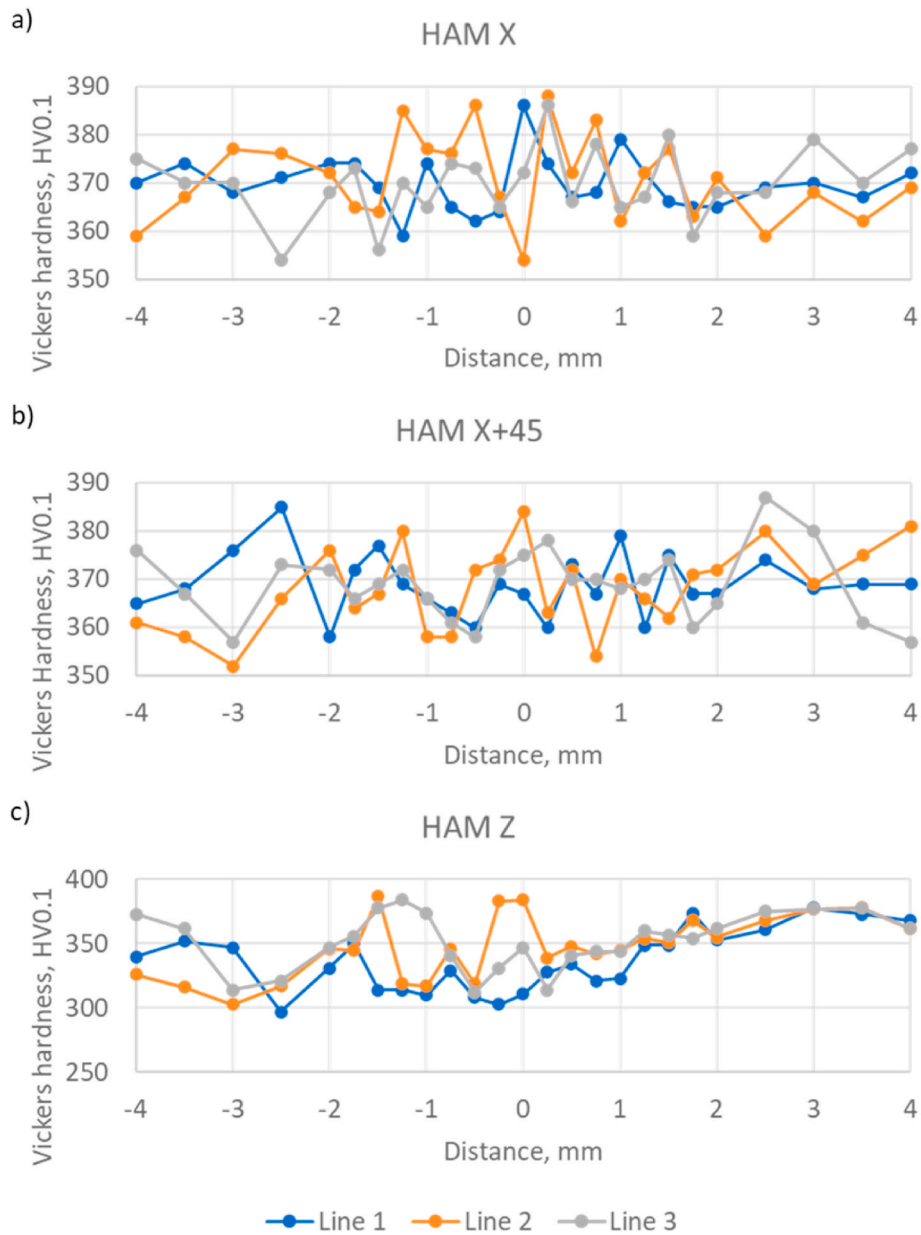
a)

b)

c)

Fig. 9. Vickers hardness profiles across the PBF/DED interface of HAM X a), HAM X+45 b), and HAM Z c) sample.

yield strength of the DED and PBF parts built in the X orientation is 1034 ± 2.7 and 1029 ± 3.3 MPa, respectively. Hence, there is only 5 MPa of difference. However, it appears that the properties of the DED in the HAM X samples are lower than the DED X samples. The average yield strength of the HAM X samples was 991 ± 8.2 MPa. Due to the poorer mechanical properties of the DED part, most of the plastic deformation occurred on the DED side, while the interface and the PBF part deformed to a lesser extent.

The third case occurs when the yield strengths of the DED and PBF parts are far apart. According to the tensile test (Fig. 11), the yield strengths of the DED and PBF parts built in the Z orientation are 932 ± 8.3 and 1028 ± 6.6 MPa, respectively. However, due to the coarse α+β microstructure and large columnar grains, the yield strength of the DED part in the HAM sample (804 ± 2.9 MPa, HAM Z, Fig. 11) is much lower than the yield strength of the PBF part. Therefore, only the DED part was deformed, while the PBF part was deformed only elastically. Points 3 and 4 (Fig. 15c) HAM Z sample) have more-or-less straight lines.

4. Discussion

4.1. Properties of PBF and DED samples

The major difference between PBF and DED process are connected to process parameters. When compared, PBF and DED processes have vastly different specific energy densities (E = P/htv, P … Laser power, h … hatch spacing, t … layer thickness, and v … scanning speed). The specific energy density of PBF and DED are E_{PBF} = 55.5 kJ/cm^3 and E_{DED} = 161 × 10^3 kJ/cm^3. There is roughly a factor of 3000x difference between PBF and DED technology. The process parameters directly influence the microstructure and tensile properties. The tensile properties of Ti6Al4V produced by AM technologies are connected to several microstructural features. Defects, prior β-grain size, shape, α-phase size, and shape have significant influence [28,38,39].

The microstructure examination of PBF and DED samples (Fig. 4) showed some variation in microstructures in terms of α-lath size (Supplementary Figs. S2 and S3) between different technology and orientation (especially DED Z and PBF Z). According to the microstructure
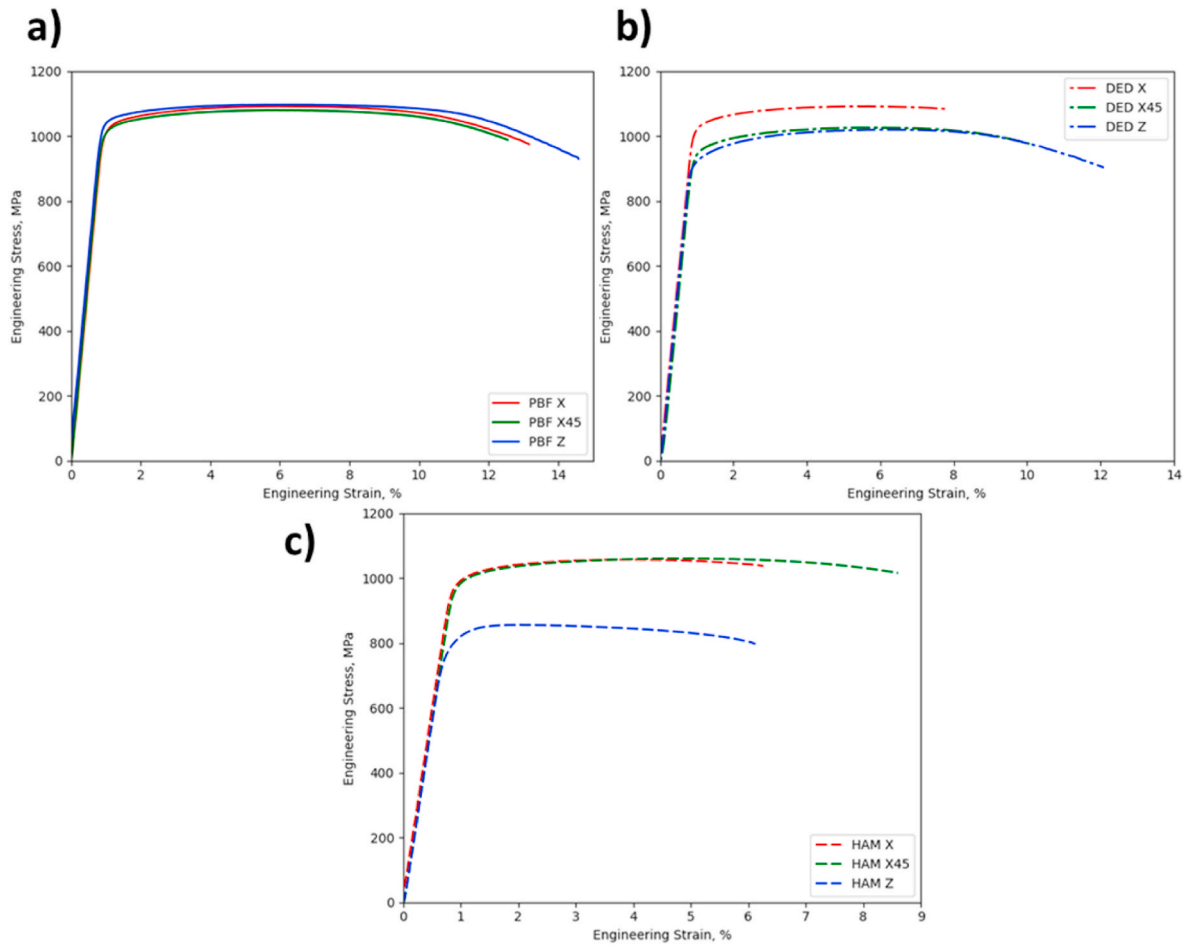
Fig. 10. Typical tensile curves for PBF a), DED b), and HAM samples c) in X, X+45, and Z orientations.
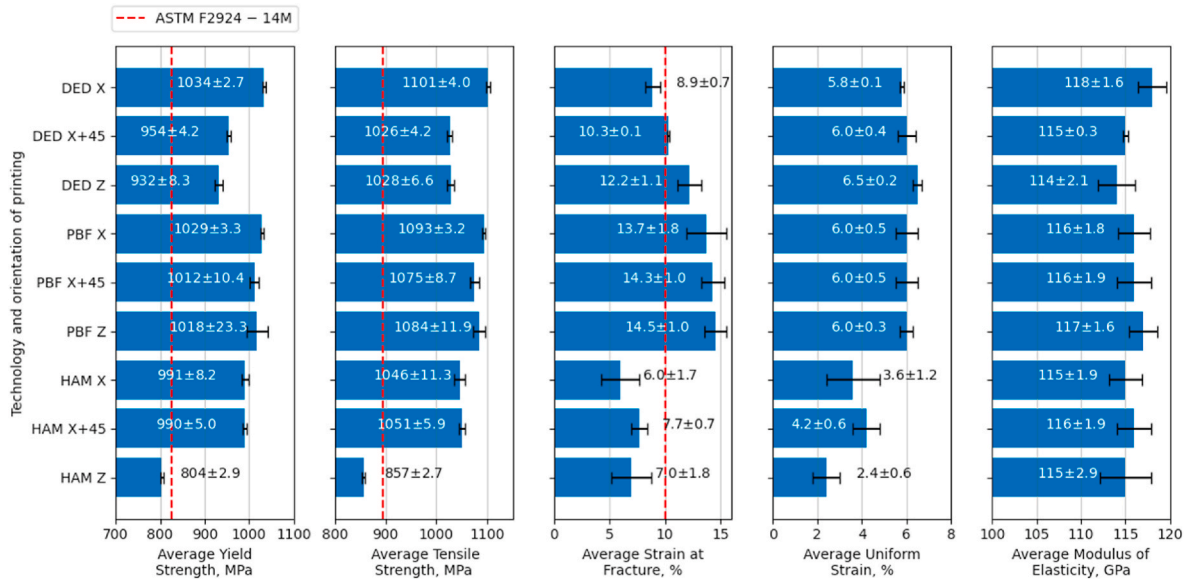

Fig. 11. Average yield strength, tensile strength, strain at fracture, uniform strain, and modulus of elasticity of DED, PBF, and HAM Ti6Al4V parts build in the X, X+45, and Z orientations.

observations and the fracture-surface examination (Fig. 4, Fig. 12, and Fig. 12a–d)), the largest differences between the PBF and DED are the prior β-grain structure and some α-phase along the grain boundary. DED produced large columnar prior-β grains, which extend through multiple deposition layers. In addition, a thin layer of α-phase along the prior-β grain boundary was seen on some prior β-grain boundaries of the DED-Z samples (Fig. 4f)).

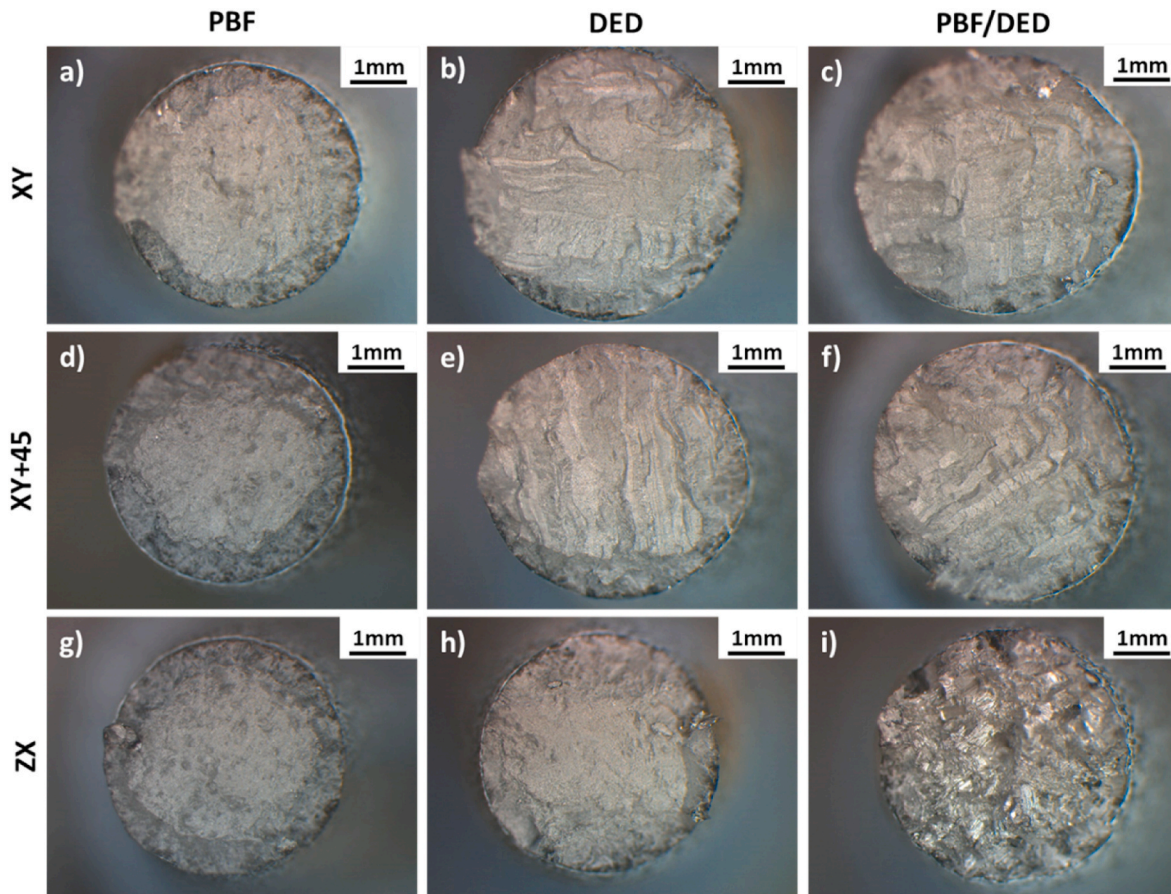The mechanical properties of the DED samples strongly depended on

Fig. 12. Stereomicroscope images of fracture surface from PBF DED and HAM samples in X, Y, and Z orientation.

texturing related to the build direction (Supplementary Figs. S5 and S6). DED X showed the highest yield (1034 ± 2.7 MPa) and tensile strengths (1101 ± 4.0 MPa), comparable to the PBF samples (Fig. 11). However, the strain at fracture was low (8.9 ± 0.7%) below 10% and outside the ASTM F2924-14 M standard for PBF, although it was still higher than the requirement stated in the ECSS-Q-ST-70-80C standard [40]. In the vertical orientation, the DED Z samples had a lower yield strength (932 ± 8.3 MPa) and tensile strength (1028 ± 6.6 MPa) but higher strain at fracture (12.2 ± 1.1%). According to the fracture surface (Fig. 12 a, d, and g)), the PBF samples have a typical cup-shaped ductile fracture with a relatively rough surface. The features observed on the DED X and X+45 samples are different. A cone-shaped fracture surface was observed, with a relatively flat central part with parallel wavy bands (Fig. 12 b and e)). The wavy bands are columnar prior β-grains. Columnar prior β-grains are large and small in numbers, so there is not much strengthening from differently oriented grains. Furthermore, the width of the columnar prior β-grains in DED parts is much wider than in the PBF parts (Fig. 6). The load direction is perpendicular to the columnar prior β-grain boundaries. The same wavy bands observed on the DED X and DED X+45 samples were not observed on the fracture surface of the DED Z samples. The fracture-surface features observed on DED Z are closer to the PBF samples. The loading direction is in the same direction as the growth of the columnar grains, resulting in a higher strain at fracture. However, such a microstructure has a lower strength (DED Z, Fig. 11). Columnar prior-β grain structures are the leading cause of mechanical anisotropy of the DED samples. The yield and average tensile strengths of the DED X samples are 9% and 7% more than in the DED Z samples, respectively, while the strain at fracture is 37% lower in the DED X samples compared to the DED Z samples. The percentages observed here are similar to observations in the literature [28]. Defects (lack-of-fusion and gas porosity) have a small role since the density of the DED samples is high, similar to the PBF samples (Fig. 2). Furthermore, only a small number of defects were observed on the fracture surface (Fig. 13a–d)).

The high strength of the PBF samples and low mechanical anisotropy is connected to the smaller size and more irregular-shaped prior β-grains compared to the DED parts. High strength and low mechanical anisotropy relate to the printing parameters (Table 3), specifically to the layer thickness and the rotation between each layer (0.03 mm and 67°, respectively). This well-known phenomenon is connected to the breakup of a straight columnar prior β-grain structure [41]. The same can be observed from the EBSD images, where the irregular shape of the prior β-grains can be seen on the PBF side (Fig. 7a)). So, of the tested technologies, the PBF samples proved to have better mechanical properties than the DED samples and those built with the HAM approach. The PBF samples showed a combination of a high average strain at fracture (13.7–14.5%), yield strength (1012–1029 MPa), and tensile strength (1075–1093 MPa) (Fig. 11). The tensile properties of PBF samples are similar to other investigations employing a similar heat-treatment regime [39] and fulfill min. requirements stated by the ASTM F2924-14 M [37] and ECSS-Q-ST-70-80C standard [42].

4.2. Properties of HAM samples

According to results and previous investigation on Inconel 718 [6], the DED side of HAM X, X+45, and Z to DED samples shows the effects of heat flow "dimensionality", the influence of interlayer dwell time, especially for Ti alloys that have a low thermal diffusivity ($\alpha = k/\rho C_p$).

For the DED part, quasi 3D heat flow dominates, and the interlayer dwell time (time between beam interaction at a given (x,y) point in one layer to the time until the beam arrives at the same point again in the next layer) is longer. These conditions tend to limit the extent of heat
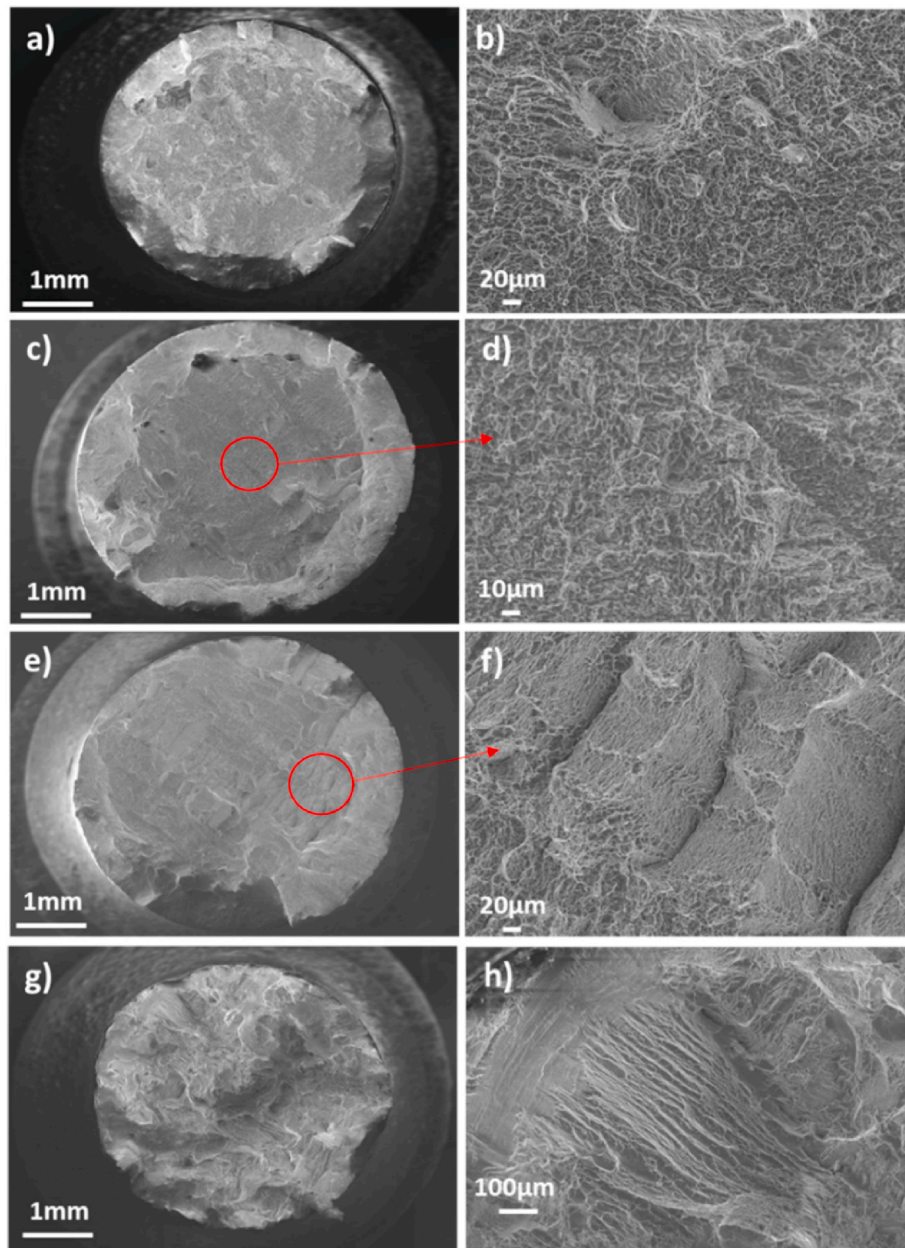
Fig. 13. SEM micrographs of fracture surface from PBF X a) and b), DED X c) and d), HAM X+45 e) and f) and HAM Z g) and h) samples.

accumulation, which keep both the thermal gradient and cooling rate high (through Fourier's laws) and limit the increase in peak temperature with build height. This is assured by wider area builds like DED X and X+45 samples or by building multiple samples at the same time for DED Z.

When the sample dimensions are reduced in our case DED side of HAM samples in comparison to full DED samples. The dimensions for HAM X and X+45 are reduced by a factor of 2 and for Z dimension by a factor of 6. The reduction in sample dimension accelerates the extent of heat accumulation, which keep both the thermal gradient and cooling rate lower (through Fourier's laws) and promote the increase in peak temperature with build height. For HAM Z samples, quasi 1D heat flow dominated, the interlayer dwell time is relatively short due to Z » radius, and the higher peak T causes large columnar grains.

The tensile properties of the HAM samples are not like the DED samples. The HAM X samples had a lower yield strength than the PBF and DED X samples (Fig. 11), whereas the yield strength of the HAM X+45 samples was between the DED and PBF samples. The variations in

strength in contrast to the DED samples are likely connected to the variations in microstructure (Fig. 5, Supplementary Figs. S2 and S3) and macro-/micro-defects (Fig. 3 and Supplementary Fig. S10). Variation in microstructure features (alpha lath thickness and α-grain boundary) compared to DED samples likely caused a different mechanical performance of HAM samples caused by size reduction. In a normal situation, cooling across the β-transus causes diffusionless transformation of the β-phase to the α'/α microstructure. The α'-phase is a mixture of plate martensite and twin martensite structures [29,30]. When the cooling rate is critical or below, the α-phase can form along the columnar prior β-grain boundary due to heterogeneous nucleation, as can be seen from some LM images on the DED side of the HAM samples. According to LM images, an α-phase layer at prior-β columnar boundaries is thick and well-defined (DED side HAM X Fig. 5b)) compared to DED samples. Furthermore, there are fractures along the grain boundaries observed on the fracture surface of HAM X (Fig. 13e and f)). During tensile loading, the columnar prior β-grain boundaries are loaded in tensile/opening mode. Because the α-phase coats a part of the columnar prior β-grain
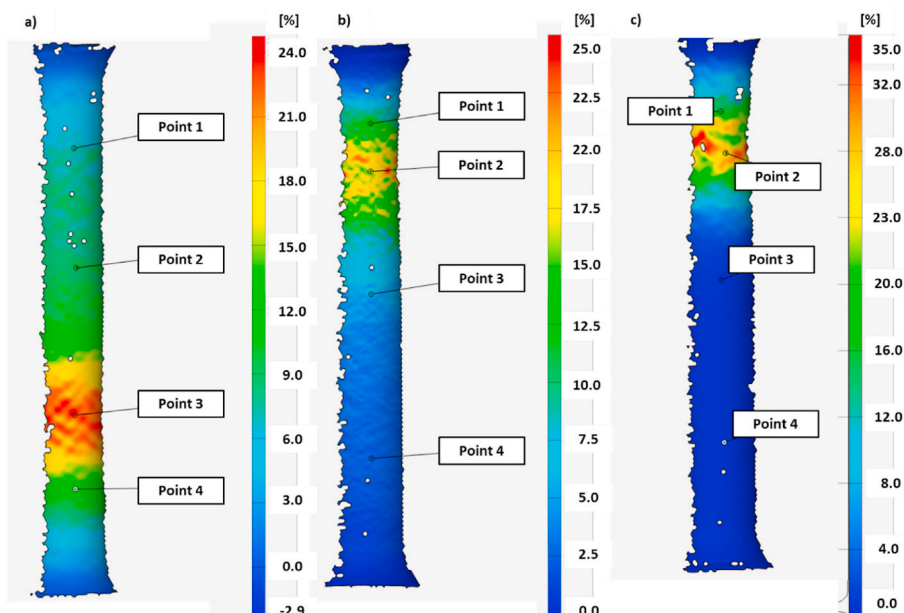
Fig. 14. Longitudinal strain distribution on PBF X, HAM X, and HAM Z samples before fracture.
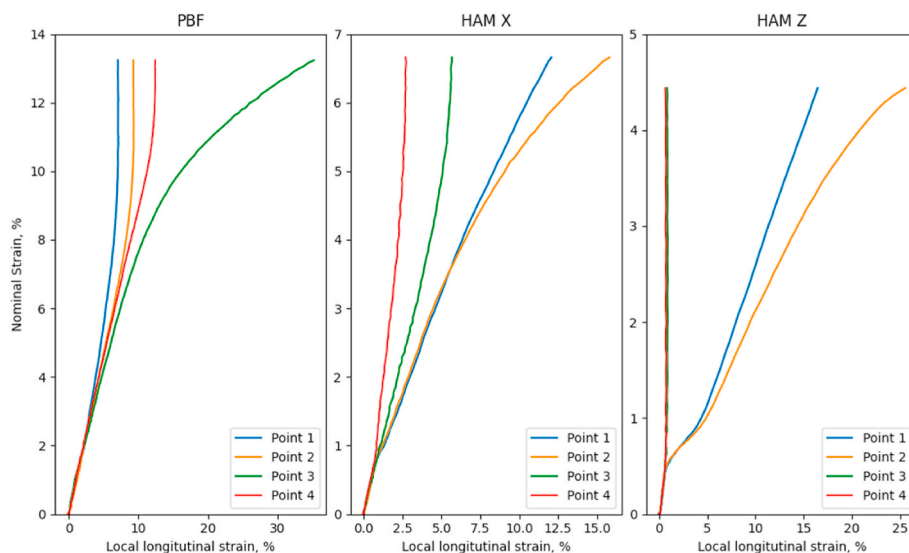

Fig. 15. Local longitudinal strain evolution vs. nominal strain of the PBF X, HAM X, and HAM Z samples.

boundary, they act as a weak point for a fracture [43].

The average yield strength and tensile strengths of the HAM X and HAM X+45 samples were similar to or lower than the DED. The average yield strength and tensile strength of the HAM X and HAM X+45 samples were around 991 MPa and 1048 Mpa, respectively. The α-lath size of HAM X samples was similar to the PBF and DED samples (Supplementary Figs. S2 and S3 and Fig. 5). This was not the case for the HAM X+45 and is likely contributing to different strength (Supplementary Figs. S2 and S3). The hardness measurements (360–375 HV0.1, Fig. 9a and b)) from the DED and PBF sides are similar to the literature, given the heat treatment applied and the resulting microstructure [44,45].

The HAM approach has an impact on the strain at fracture (HAM X 6.0 ± 1.7%, HAM X+45 7.7 ± 0.7%, and HAM Z 7.0 ± 1.8%). The main contribution to lowering the fracture strain comes from the difference in material properties between PBF and DED. In theory (when a homogeneous material is tested), we have three district regions in the tensile curve (Fig. 15a)). These are the elastic and homogeneous plastic

deformation regions that follow into the necking and fracture. Strain at fracture is defined as the ratio between the difference in the length after rupture of the test specimen and the initial length (gauge length). The change in length depends on the condition that the whole specimen will deform uniformly throughout the gauge section. However, this condition never occurs (Fig. 15 b) and c)) when one part of the sample has better material properties (PBF) and the others have poorer properties (DED) [3–5,32]. Localized plastic deformation will happen in the part of the sample with the softest properties (the lowest yield strength DED, Fig. 11 and Fig. 15). Because of this, there is no region of homogeneous plastic deformation after the yield point (Fig. 15b)) as opposed to the PBF (Fig. 15a)) or DED samples. Furthermore, the softer part is distributed in a short length of the gauge section thus the uniform strain will be much lower (Supplementary Fig. S11). Strain is accumulated in the DED part, limited on one side by fillets and on the other side by a stronger PBF/DED interface. According to ASTM F2924-14 [37], the HAM samples do not meet the standard's requirements, as they all had a

strain at fracture below 10% even when compared to ECSS-Q-ST-70-80C [40], where the strain at fracture should be above 8%.

Hardness profiles across the PBF/DED interface of HAM X and XY samples show little evidence of a heat-affected zone (Fig. 9a and b)). High temperatures caused by the laser result in a steep temperature gradient in the melt pool. During the DED process, direct epitaxial grain growth of columnar β grains from the parent PBF grains at the pool bottom is favored over nucleation [46]. Thus, only a transition from the small-grained PBF structure to the columnar prior β-grain structure is visible (Fig. 7). There is no notable grain growth in the PBF part near the fusion line since they are likely stable. Furthermore, during the cooling period, the melt pool and PBF part are exposed to the same cooling rate and adopt the same fine α'/α microstructure (before heat treatment was applied). Due to epitaxial growth, multiple columnar prior β-grains grow from the parent PBF grains (Fig. 6 and 7). In the HAM X and X+45 samples, the prior-β columnar grains were slightly angled toward the interface, likely due to heat conduction into the PBF part. Away from the interface region, prior-β columnar grains align in the build direction (Z).

Heat accumulation in HAM Z samples was extensive causing a severe reduction in strength. When the cooling rate across β-transus is very slow, the β-phase transforms into α-lamella colonies. The α-lamella colonies typically grow from the edge of the prior β-grains towards the other obstruction like other α-lamella colonies or grain boundary (Fig. 5f). In addition, the columnar prior β-grain boundaries had a layer of α-phase. The extensive heat input caused by short interlayer dwell time formed a sizeable heat-affected zone (about 3 mm thick). The heat-affected area is seen in images from the microstructure examinations (Fig. 6c) and Supplementary Figs. S7a and b)) and Vickers hardness profile (Fig. 9c). A rough α+β microstructure composed of large α-phase lamella colonies has lower strength compared to the fine α+β microstructure of DED and HAM X and XY samples (Fig. 11).

4.3. Defects at the PBF/DED interface of HAM samples

Some HAM X and X+45 samples had severe defects at the PBF/DED interface (Fig. 3a and b) and Supplementary Figs. S14). CT scans of the HAM X and X+45 samples (Fig. 3a and b)) showed two types of defects at the PBF/DED interface. Both types of defects are aligned with the angled surface of the PBF part. The first defects are minor in size with a mostly spherical shape (mostly colored blue in Fig. 3a–d)). The rough PBF surface could be a source of gas bubbles upon remelting due to the different thermal conditions. The second type of defect is large lack-of-fusion defects. The deposition of a geometrically desired laser track free of defects is an interplay of process parameters, thermal history, substrate temperature, gas flow rate, and surface state [47]. The substrate is initially "cold" at the start of deposition, and 3D heat flow conditions exist. These conditions tend to cause increased heat loss to the substrate by conduction and leave less heat energy to melt the substrate and powder, resulting in melt pool dimensions smaller than found after the thermal transient. In turn, the smaller dimensions result in insufficient hatch and layer overlap and can form lack-of-fusion defects observed here (Fig. 3a–d)). The initial cold thermal transient at the start of the DED deposition likely caused defects in the lower 1/3 of the HAM X+45 sample (Fig. 3c and d)). The process parameters (power, scan rate, and powder feed rate) must be optimized locally (in the transition zone), to reduce the probability of the lack-of-fusion defect formation. In addition, cleaning, potential oxide formation, and pick up of moisture could contribute to the defects, most prominently in the HAM samples.

5. Conclusions

Our parts were produced using a hybrid PBF + DED approach in different orientations (two horizontal and one vertical). The tensile tests were conducted on parts built with the individual PBF and DED processes, as well as the hybrid additive manufacturing (HAM) approach. A comparison of the tensile properties of the parts and observations relating to their microstructures and defects allowed us to draw the following conclusions.

- The HAM Ti6Al4V parts have a strong PBF/DED interface and preferentially fracture on the weaker DED. A strong interface was obtained despite DED on the as-built PBF surface. This opens the possibility of avoiding machining between PBF and DED processes when building HAM parts. The microstructure of a typical interface exhibited porosity, which should be considered in fatigue-sensitive applications.
- There were exceptions regarding the fracture site in the horizontal HAM parts. A few horizontal HAM parts developed lack-of-fusion defects and thus fractured at the PBF/DED interface. The laser scanning path dictated the size and shape of the lack-of-fusion defects during the DED process. The more significant defects were smaller in the horizontal HAM X+45 parts (parts rotated 45° about the z-axis). DED process parameters at the interface should be optimized and the quality of the deposition surface before DED should be controlled, to reduce the probability of defect formation at the PBF/DED interface.
- The HAM parts built in the horizontal orientation had intermediate tensile strengths (horizontal about 1048 MPa) in line with standards like ASTM F2924-14. However, in the case of the vertical parts, the tensile strength (857 MPa) was much lower than for the DED parts (1026–1101 MPa). Regarding potential future designs with HAM, DED on angled interfaces offers many new possibilities. However, parts with a limited cross-section (especially $<10^2$ mm^2) present two difficulties. HAM test parts DED processed with a limited cross-section will have significantly lower tensile properties (far below ASTM F2924-14). Designs should avoid having sections with small cross-sections when using HAM with PBF and DED.
- The HAM approach significantly impacted the strain at fracture. The average strain at a fraction of a single process was often far more (DED> 8% and PBF >12%), while the HAM parts were below 8% (HAM X 6.0 ± 1.7%, HAM X+45 7.7 ± 0.7%). Due to the localized deformation (on the DED side) during the tensile test, the strains at fracture of the HAM X and HAM X+45 parts were lower.
- DED processing of all the HAM parts showed a heat-flow restriction following the thermal evolution. A different thermal evolution leads to different melt-pool dimensions, critical or below-critical cooling rates, and heat accumulation, which promotes the formation of undesirable defects and microstructure as well as sub-par mechanical properties.

CRediT authorship contribution statement

Simon Malej: Funding acquisition, Project administration, Data curation, Formal analysis, Investigation, Methodology, Visualization, Writing – original draft. **Matjaž Godec:** Funding acquisition, Supervision, Investigation, Writing – review & editing. **Črtomir Donik:** Methodology, Writing – review & editing. **Matej Balazic:** Funding acquisition, Project administration, Conceptualization, Supervision, Resources, Writing – review & editing, Resources, Writing – review & editing. **René Zettler:** Resources, Writing – review & editing. **Thomas Lienert:** Resources, Writing – review & editing. **Laurent Pambaguian:** Supervision, Writing – review & editing.

Declaration of competing interest

The authors declare that they have no known competing financial interests or personal relationships that could have appeared to influence the work reported in this paper.

Data availability

Data will be made available on request.

Appendix A. Supplementary data

Supplementary data to this article can be found online at https://doi.org/10.1016/j.msea.2023.145229.

References

[1] M.E. Korkmaz, S. Waqar, A. Garcia-Collado, M.K. Gupta, G.M. Krolczyk, A technical overview of metallic parts in hybrid additive manufacturing industry, J. Mater. Res. Technol. 18 (2022) 384–395, https://doi.org/10.1016/J.JMRT.2022.02.085.

[2] W.-S. Woo, E.-J. Kim, H.-I. Jeong, C.-M. Lee, Laser-assisted machining of Ti-6Al-4V fabricated by DED additive manufacturing, Int. J. Precis. Eng. Manuf. Green Technol. 7 (2020) 559–572, https://doi.org/10.1007/S40684-020-00221-7, 3. 7 (2020).

[3] M. Bambach, I. Sizova, B. Sydow, S. Hemes, F. Meiners, Hybrid manufacturing of components from Ti-6Al-4V by metal forming and wire-arc additive manufacturing, J. Mater. Process. Technol. 282 (2020), https://doi.org/10.1016/J.JMATPROTEC.2020.116689.

[4] O. Dolev, S. Osovski, A. Shirizly, Ti-6Al-4V hybrid structure mechanical properties—wrought and additive manufactured powder-bed material, Addit. Manuf. 37 (2021), 101657, https://doi.org/10.1016/J.ADDMA.2020.101657.

[5] X. Shi, S. Ma, C. Liu, Q. Wu, J. Lu, Y. Liu, W. Shi, Selective laser melting-wire arc additive manufacturing hybrid fabrication of Ti-6Al-4V alloy: microstructure and mechanical properties, Mat. Sci. Eng. A 684 (2017) 196–204, https://doi.org/10.1016/J.MSEA.2016.12.065.

[6] M. Godec, S. Malej, D. Feizpour, Č. Donik, M. Balažic, D. Klobčar, L. Pambaguian, M. Conradi, A. Kocijan, Hybrid additive manufacturing of Inconel 718 for future space applications, Mater. Char. 172 (2021), 110842, https://doi.org/10.1016/j.matchar.2020.110842.

[7] E. Uhlmann, T. Düchting, T. Petrat, E. Krohmer, B. Graf, M. Rethmeier, Effects on the distortion of Inconel 718 components along a hybrid laser-based additive manufacturing process chain using laser powder bed fusion and laser metal deposition, Prog. Addit. Manuf. 6 (2021) 385–394, https://doi.org/10.1007/S40964-021-00171-9.

[8] M. Kumaran, V. Senthilkumar, Influence of heat treatment on stainless steel 316L alloy manufactured by hybrid additive manufacturing using powder bed fusion and directed energy deposition, Met. Mater. Int. (2022) 1–18, https://doi.org/10.1007/S12540-022-01225-5.

[9] A. Kudzal, B. McWilliams, C. Hofmeister, F. Kellogg, J. Yu, J. Taggart-Scarff, J. Liang, Effect of scan pattern on the microstructure and mechanical properties of Powder Bed Fusion additive manufactured 17-4 stainless steel, Mater. Des. 133 (2017) 205–215, https://doi.org/10.1016/J.MATDES.2017.07.047.

[10] N. Sanaei, A. Fatemi, Analysis of the effect of surface roughness on fatigue performance of powder bed fusion additive manufactured metals, Theor. Appl. Fract. Mech. 108 (2020), 102638, https://doi.org/10.1016/J.TAFMEC.2020.102638.

[11] B. Barroqueiro, A. Andrade-Campos, R.A.F. Valente, V. Neto, Metal additive manufacturing cycle in aerospace industry: a comprehensive review, J. Manuf. Mater. Process. 3 (2019) 52, https://doi.org/10.3390/jmmp3030052.

[12] N. Kladovasilakis, P. Charalampous, I. Kostavelis, D. Tzetzis, D. Tzovaras, Impact of metal additive manufacturing parameters on the powder bed fusion and direct energy deposition processes: a comprehensive review, Prog. Addit. Manuf. 6 (2021) 349–365, https://doi.org/10.1007/S40964-021-00180-8.

[13] A. Khorasani, I. Gibson, J. Kozhuthala Veetil, & Amir, H. Ghasemi, A review of technological improvements in laser-based powder bed fusion of metal printers, (n.d.). https://doi.org/10.1007/s00170-020-05361-3.

[14] S. Gruber, C. Grunert, M. Riede, E. López, A. Marquardt, F. Brueckner, C. Leyens, Comparison of dimensional accuracy and tolerances of powder bed based and nozzle based additive manufacturing processes, J. Laser Appl. 32 (2020), 032016, https://doi.org/10.2351/7.0000115.

[15] Y. Zhang, L. Wu, X. Guo, S. Kane, Y. Deng, Y.G. Jung, J.H. Lee, J. Zhang, Additive manufacturing of metallic materials: a review, J. Mater. Eng. Perform. 27 (2018) 1–13, https://doi.org/10.1007/S11665-017-2747-Y.

[16] Optomec Inc., Lens 1500 additive manufacturing controlled atmosphere system, n. d. https://optomec.com/wp-content/uploads/2018/11/LENS-1500-AM-CA_WEB1018.pdf. (Accessed 31 May 2022).

[17] H. Siva Prasad, F. Brueckner, A.F.H. Kaplan, Powder incorporation and spatter formation in high deposition rate blown powder directed energy deposition. https://doi.org/10.1016/j.addma.2020.101413, 2020.

[18] K. Vartanian, L. Brewer, K. Manley, T. Cobbs, POWDER BED FUSION vs. DIRECTED ENERGY DEPOSITION BENCHMARK STUDY: MID-SIZE PART with SIMPLE GEOMETRY. https://www.optomec.com/wp-content/uploads/2018/06/PBF-vs-DED-BENCHMARK-STUDY_7March_2018-03.pdf, 2018. (Accessed 1 June 2022).

[19] J. Wang, X. Zhou, J. Li, J. Zhu, M. Zhang, A comparative study of Cu–15Ni–8Sn alloy prepared by L-DED and L-PBF: microstructure and properties, Mat. Sci. Eng. A 840 (2022), 142934, https://doi.org/10.1016/J.MSEA.2022.142934.

[20] H.W. Jones, The recent large reduction in space launch cost, 48th international conference on environmental systems. https://ttu-ir.tdl.org/bitstream/handle/2346/74082/ICES_2018_81.pdf?sequence=1, 2018. (Accessed 9 June 2022).

[21] Thomas G. Roberts, Space Launch to Low Earth Orbit: How Much Does it Cost? - Aerospace Security, Center for Strategic and International Studies, 2020. https://aerospace.csis.org/data/space-launch-to-low-earth-orbit-how-much-does-it-cost/. (Accessed 9 June 2022).

[22] M. Donachie, Titanium: A Technical Guide, ASM International, 2000.

[23] V. Anil Kumar, R.K. Gupta, M.J.N.V. Prasad, S.V.S. Narayana Murty, Recent advances in processing of titanium alloys and titanium aluminides for space applications: a review, J. Mater. Res. 36 (2021) 689–716, https://doi.org/10.1557/s43578-021-00104-w.

[24] M. Jackson, K. Dring, A Review of Advances in Processing and Metallurgy of Titanium Alloys, 2013, pp. 881–887, https://doi.org/10.1179/174328406X111147, 10.1179/174328406X111147. 22.

[25] M.T. Tsai, Y.W. Chen, C.Y. Chao, J.S.C. Jang, C.C. Tsai, Y.L. Su, C.N. Kuo, Heat-treatment effects on mechanical properties and microstructure evolution of Ti-6Al-4V alloy fabricated by laser powder bed fusion, J. Alloys Compd. 816 (2020), 152615, https://doi.org/10.1016/J.JALLCOM.2019.152615.

[26] P. Kumar, U. Ramamurty, Microstructural optimization through heat treatment for enhancing the fracture toughness and fatigue crack growth resistance of selective laser melted Ti–Al–4V alloy, Acta Mater. 169 (2019) 45–59, https://doi.org/10.1016/j.actamat.2019.03.003.

[27] S.M.J. Razavi, F. Berto, Directed energy deposition versus wrought Ti-6Al-4V: a comparison of microstructure, fatigue behavior, and notch sensitivity, Adv. Eng. Mater. 21 (2019), 1900220, https://doi.org/10.1002/ADEM.201900220.

[28] B.E. Carroll, T.A. Palmer, A.M. Beese, Anisotropic tensile behavior of Ti–6Al–4V components fabricated with directed energy deposition additive manufacturing, Acta Mater. 87 (2015) 309–320, https://doi.org/10.1016/J.ACTAMAT.2014.12.054.

[29] M.T. Tsai, Y.W. Chen, C.Y. Chao, J.S.C. Jang, C.C. Tsai, Y.L. Su, C.N. Kuo, Heat-treatment effects on mechanical properties and microstructure evolution of Ti-6Al-4V alloy fabricated by laser powder bed fusion, J. Alloys Compd. 816 (2020), 152615, https://doi.org/10.1016/j.jallcom.2019.152615.

[30] C.M. Cepeda-Jiménez, F. Potenza, E. Magalini, V. Luchin, A. Molinari, M.T. Pérez-Prado, Effect of energy density on the microstructure and texture evolution of Ti-6Al-4V manufactured by laser powder bed fusion, Mater. Char. 163 (2020), https://doi.org/10.1016/J.MATCHAR.2020.110238.

[31] S. Shrestha, R.P. Panakarajupally, M. Kannan, G. Morscher, A.L. Gyekenyesi, O. E. Scott-Emuakpor, Analysis of microstructure and mechanical properties of additive repaired Ti–6Al–4V by Direct Energy Deposition, Mat. Sci. Eng. A 806 (2021), 140604, https://doi.org/10.1016/J.MSEA.2020.140604.

[32] Y. Zhu, J. Li, X. Tian, H. Wang, D. Liu, Microstructure and mechanical properties of hybrid fabricated Ti–6.5Al–3.5Mo–1.5Zr–0.3Si titanium alloy by laser additive manufacturing, Mat. Sci. Eng. A 607 (2014) 427–434, https://doi.org/10.1016/J.MSEA.2014.04.019.

[33] (n.d. SciPy. https://scipy.org/. (Accessed 18 May 2023).

[34] Matplotlib — visualization with Python (n.d.), https://matplotlib.org/. (Accessed 18 May 2023).

[35] scipy.stats.ttest_ind — SciPy v1.10.1 Manual (n.d.), https://docs.scipy.org/doc/scipy/reference/generated/scipy.stats.ttest_ind.html. (Accessed 18 May 2023).

[36] A.S.H. Kabir, X. Cao, J. Gholipour, P. Wanjara, J. Cuddy, A. Birur, M. Medraj, Effect of postweld heat treatment on microstructure, hardness, and tensile properties of laser-welded Ti-6Al-4V, Metall Mater Trans A Phys Metall Mater Sci 43 (2012) 4171–4184, https://doi.org/10.1007/S11661-012-1230-5/FIGURES/14.

[37] Standard Specification for Additive Manufacturing Titanium-6 Aluminum-4 Vanadium with Powder Bed Fusion, (n.d.). https://www.astm.org/f2924-14r21.html (accessed May 12, 2022).

[38] W.H. Kan, M. Gao, X. Zhang, E. Liang, N.S.L. Chiu, C.V.S. Lim, A. Huang, The influence of porosity on Ti-6Al-4V parts fabricated by laser powder bed fusion in the pursuit of process efficiency, Int. J. Adv. Manuf. Technol. (2022) 1–22, https://doi.org/10.1007/S00170-021-08374-8.

[39] S.A. Etesami, B. Fotovvati, E. Asadi, Heat treatment of Ti-6Al-4V alloy manufactured by laser-based powder-bed fusion: process, microstructures, and mechanical properties correlations, J. Alloys Compd. 895 (2022), 162618, https://doi.org/10.1016/J.JALLCOM.2021.162618.

[40] ECSS-Q-ST-70-80C – Processing and Quality Assurance Requirements for Metallic Powder Bed Fusion Technologies for Space Applications, 30 July 2021. | European Cooperation for Space Standardization, (n.d.), https://ecss.nl/standard/ecss-q-st-70-80c-processing-and-quality-assurance-requirements-for-metallic-powder-bed-fusion-technologies-for-space-applications-30-july-2021/. (Accessed 2 May 2022).

[41] P. Kumar, O. Prakash, U. Ramamurty, Micro-and meso-structures and their influence on mechanical properties of selectively laser melted Ti-6Al-4V, Acta Mater. 154 (2018) 246–260, https://doi.org/10.1016/j.actamat.2018.05.044.

[42] European Cooperation for Space Standardization, ECSS-Q-ST-70-80C – Processing and Quality Assurance Requirements for Metallic Powder Bed Fusion Technologies for Space Applications, European Cooperation for Space Standardization, 30 July 2021, 2021, https://ecss.nl/standard/ecss-q-st-70-80c-processing-and-quality-assurance-requirements-for-metallic-powder-bed-fusion-technologies-for-space-applications-30-july-2021/. (Accessed 21 February 2022).

[43] P. Åkerfeldt, M.-L. Antti, R. Pederson, Influence of microstructure on mechanical properties of laser metal wire-deposited Ti-6Al-4V, Mat. Sci. Eng. A 674 (2016) 428–437, https://doi.org/10.1016/j.msea.2016.07.038.

[44] S.Q. Wu, Y.J. Lu, Y.L. Gan, T.T. Huang, C.Q. Zhao, J.J. Lin, S. Guo, J.X. Lin, Microstructural evolution and microhardness of a selective-laser-melted Ti–6Al–4V alloy after post heat treatments, J. Alloys Compd. 672 (2016) 643–652, https://doi.org/10.1016/J.JALLCOM.2016.02.183.

[45] Y. Zhai, D.A. Lados, E.J. Brown, G.N. Vigilante, Understanding the microstructure and mechanical properties of Ti-6Al-4V and Inconel 718 alloys manufactured by laser engineered net shaping, Addit. Manuf. 27 (2019) 334–344, https://doi.org/10.1016/J.ADDMA.2019.02.017.

[46] T. Wang, Y.Y. Zhu, S.Q. Zhang, H.B. Tang, H.M. Wang, Grain morphology evolution behavior of titanium alloy components during laser melting deposition additive manufacturing, J. Alloys Compd. 632 (2015) 505–513, https://doi.org/10.1016/j.jallcom.2015.01.256.

[47] T. Zhao, Y. Wang, T. Xu, M. Bakir, W. Cai, M. Wang, M. Dahmen, Q. Zheng, X. Wei, C. Hong, C. Zhong, P. Albus, T. Schopphoven, A. Gasser, C.L. Häfner, Some factors affecting porosity in directed energy deposition of AlMgScZr-alloys, Opt Laser. Technol. 143 (2021), 107337, https://doi.org/10.1016/J.OPTLASTEC.2021.107337.